processes

MDPI

Article

A Mathematical Model for Water Huff-and-Puff in Tight Oil Reservoirs Considering the Effect of Low-Salinity Water

Xiong Liu *, Yu Chen, Yirui Ren, Tuanqi Yao and Zhiyuan Du

School of Petroleum Engineering, Xi'an Shiyou University, Xi'an 710065, China
* Correspondence: liuxiong2016@xsyu.edu.cn

Abstract

To address the insufficient consideration of osmotic pressure in existing studies on water huff-and-puff in tight oil reservoirs, this paper introduces both osmotic and capillary pressures into two-phase flow theory and develops a full-cycle model for low-salinity water injection. The effects of salinity, injection rate, and soaking time on pressure, saturation, and salt concentration are analyzed. Results show that lower salinity enhances osmotic drive and improves recovery. Specifically, 1000 mg/L yields the highest recovery (10.94%) and an osmotic gradient of ~3.9 MPa. Capillary pressure acts synergistically with osmotic pressure during the soaking stage, promoting spontaneous imbibition and fluid redistribution. An optimal injection rate exists: excessive rates reduce swept volume, while very low rates prolong the cycle. Quantitatively, 80 m^3/d is preferred (recovery 10.94%) over 40 m^3/d (11.13%) as it halves the injection time with comparable recovery. There is also an optimal soaking time beyond which incremental gain diminishes. Recovery rises from 9.32% at 20 d to 10.94% at 40 d, with only 0.28% and 0.20% gains afterward; thus, 40 d is optimal. The model captures osmotic-driven behavior and reveals the secondary displacement effect during soaking, supporting parameter optimization.

Keywords: low-salinity water; tight oil reservoir; water huff-and-puff; mathematical model; parameter sensitivity analysis

1. Introduction

Water huff-and-puff is an effective method for replenishing formation energy and enhancing oil recovery in tight oil reservoirs. Laboratory experiments have confirmed that low-salinity water can further improve the huff-and-puff performance [1–3]. This technique involves multiple cycles of injection, soaking, and production operations, leveraging the physicochemical interactions between the fluid and the rock during the soaking stage to achieve pore-scale imbibition displacement [4–6]. Compared with conventional huff-and-puff, low-salinity water huff-and-puff offers advantages such as low cost, minimal formation damage, and wide applicability [7,8]. Bigdeli et al. [9] further emphasized the economic viability of low-salinity waterflooding, noting that its commercial success depends on balancing incremental oil recovery with operational costs—a consideration that is equally relevant to huff-and-puff operations.

The core of low-salinity water huff-and-puff lies in the fact that the injected water salinity is significantly lower than that of the formation water, thereby enhancing oil recovery by altering the oil–water–rock interfacial properties [10,11]. Extensive experiments have demonstrated that the low-salinity threshold generally falls within the range of 1000–5000 mg/L [12]. Nyah et al. [13] comprehensively reviewed the role of

Check for updates

Academic Editors: Chuanjin Yao and Qingbang Meng

Received: 25 May 2026
Revised: 19 June 2026
Accepted: 29 June 2026
Published: 1 July 2026

Copyright: © 2026 by the authors. Licensee MDPI, Basel, Switzerland. This article is an open access article distributed under the terms and conditions of the Creative Commons Attribution (CC BY) license.

salinity on oil recovery mechanisms during chemical flooding, noting that optimal salinity thresholds for augmenting recovery typically fall within 1000–6000 ppm, which is consistent with the 1000 mg/L optimal value identified in our study. Salinity and ionic composition are key parameters governing interfacial interactions; reducing salinity or optimizing ionic composition can both improve the ultimate oil recovery [14–16]. Mechanisms widely discussed to date include wettability alteration, electrical double-layer expansion, multi-component ion exchange, alkaline-like flooding, fines migration, and osmotic pressure [17–19]. Arain et al. [20] recently provided a state-of-the-art review on synergising nanoparticles and low-salinity waterflooding, highlighting the potential of hybrid approaches for enhanced oil recovery. Among these, surface chemistry effects such as wettability alteration and ion exchange have received considerable attention during the injection stage [19,21]. However, during the soaking stage, as forced convection essentially ceases, osmotic pressure driven by the salinity gradient may play a dominant role in controlling fluid redistribution and residual oil displacement as a secondary physical displacement mechanism, yet it has thus far received insufficient attention [22,23].

The osmotic pressure effect arises from the salinity difference between the injected water and the formation water. The semi-permeable membrane-like behavior of the porous rock medium can generate an osmotic pressure difference across it, which disrupts the adsorption equilibrium of crude oil on pore surfaces, drives water molecules to diffuse through the oil into low-permeability zones, and thereby improves oil displacement efficiency [24,25]. Sandengen et al. [26] first explicitly proposed osmotic pressure as an independent oil-displacement mechanism under low-salinity conditions, and experimentally demonstrated that oil droplets can act as semi-permeable membranes to imbibe water, swell, and migrate. Fredriksen et al. [27] directly observed the mobilization of residual oil and capillary-trapped oil under a salinity gradient using micromodel visualization techniques, confirming the synergistic effects of osmosis and diffusion at the pore scale. Fakcharoenphol et al. [28] noted that in fractured shale reservoirs, low-salinity water can enter the matrix through osmosis and displace oil by countercurrent flow. Huang et al. [29] further revealed that under low-salinity conditions, oil droplet swelling is driven by osmotic pressure and depends on the presence of oil-soluble surfactants and initial water content. Zhao et al. [30] proposed a spontaneous imbibition mechanism driven by the coupling of osmotic pressure and interfacial tension gradients for oil-wet tight reservoirs. Takeda et al. [31] measured an osmotic pressure as high as 37 kPa in in situ experiments on oil-bearing sandstone, confirming the significant contribution of chemical osmosis to the directed migration of crude oil. Bui and Tutuncu [32] demonstrated through simulations that concentration-gradient-driven osmotic transport makes a non-negligible contribution to oil recovery in unconventional reservoirs. Fan et al. [33] systematically investigated the mechanisms and laws of low-salinity water flooding in tight sandstone reservoirs using contact angle, core displacement, ion chromatography, and NMR experiments, providing direct experimental evidence that complements our numerical simulation results. Wang et al. [34] further demonstrated the applicability of low-salinity waterflooding in heavy oil sandstone reservoirs, offering additional insights into oil recovery efficiency and mechanisms across different reservoir types. Collectively, these studies indicate that osmotic pressure, as a secondary displacement mechanism during the soaking stage, plays an irreplaceable physical role in the low-salinity water huff-and-puff process and urgently needs to be quantitatively described in huff-and-puff simulation [35].

In terms of modeling, early mathematical models largely simplified the low-salinity effect as a shift in relative permeability curves or a reduction in residual oil saturation [36]. In recent years, ion-exchange models have become the mainstream approach, as they are capable of explaining the incremental oil recovery resulting from wettability alteration [37,38].

Omekeh et al. [37] developed a mathematical model that accounts for ion exchange and mineral dissolution. Apolinário and Pires [38] proposed a low-salinity-effect model for sandstone reservoirs based on multi-component cation exchange. Jalilian et al. [39] recently conducted a comparative study assessing the impact of different geochemical mechanisms—including fines migration, rock dissolution/precipitation, and multi-ion exchange—on the precision of low-salinity waterflooding modelling, providing useful benchmarks for model selection. Liu et al. [40] developed a pore-scale model of low-salinity water flooding in porous media using the lattice Boltzmann method, enabling multi-physics coupling simulation at the pore level. Alvarez et al. [41] proposed a numerical model for low-salinity carbonated water flooding that accounts for surface complexes and geochemical reactions, offering a comprehensive framework for modeling low-salinity effects in carbonate reservoirs. However, none of the above models incorporate the osmotic pressure term. As a body force, osmotic pressure plays a critical role during the soaking stage when forced convection is absent, governing fluid redistribution and residual oil displacement. Neglecting osmotic pressure leads to inaccurate predictions of water saturation evolution during the soaking period, thereby compromising the reliability of recovery evaluation [42]. Gbadamosi et al. [43] comprehensively reviewed recent advances in low-salinity waterflooding and chemical enhanced oil recovery, further underscoring the importance of integrating multiple mechanisms—including osmotic pressure—into predictive models for improved recovery.

In summary, existing models focus predominantly on ion exchange and wettability alteration, while the osmotic pressure effect has not yet been incorporated into the huff-and-puff simulation framework. This gap is particularly significant because, during the soaking stage when forced convection ceases, osmotic pressure, together with capillary pressure, governs fluid redistribution and residual oil displacement—neglecting it would lead to inaccurate predictions of water saturation evolution and recovery evaluation. To address this issue, this paper introduces the osmotic pressure term and the capillary pressure term into the oil–water two-phase flow theory and establishes a mathematical model for water huff-and-puff in tight oil reservoirs considering the effect of low-salinity water. The model is solved using block-centered grid discretization and the IMPES method, enabling full-life-cycle simulation of injection, soaking, and production. The influences of injected-water salinity, injection rate, and soaking time on the distributions of pore pressure, water saturation, and salt concentration are systematically analyzed, and the dominant role of osmotic pressure at different huff-and-puff stages is clarified.

2. Materials and Methods

As shown in Figure 1, the surfaces of rock grains in tight reservoirs are negatively charged and adsorb cations from the aqueous solution, forming a diffuse double layer that endows the pore space with a semi-permeable membrane-like characteristic. When low-salinity water is injected into a high-salinity formation, a concentration difference is established within the pores, causing water molecules to spontaneously diffuse from the low-salinity side to the high-salinity side. This process generates osmotic pressure, which acts as an additional driving force for fluid flow. The formula described by Marine et al. [44] for osmotic pressure generated by salinity differences:

$$\pi = \frac{RT_{\mathrm{res}}}{V} \ln\left(\frac{a_{\mathrm{wI}}}{a_{\mathrm{wII}}}\right) \tag{1}$$

where π is osmotic pressure, Pa; R is the universal gas constant, 8.314 J·mol^{-1}·K^{-1} (or 0.082 L·atm·mol^{-1}·K^{-1}, depending on the units used for pressure and volume); T_{res} is

temperature, K; V is water molar volume, m^3/mol; a_{wI} is water activity of low salinity solution, dimensionless; a_{wII} is water activity of high salinity solution, dimensionless.

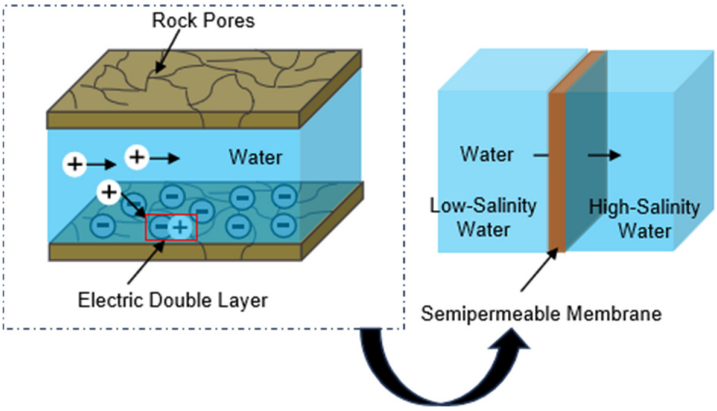


Figure 1. Generation mechanism of osmotic pressure.

Following the classical Corey-type models (Corey, 1954; Brooks and Corey, 1964), the oil–water two-phase relative permeability and capillary pressure functions are expressed as [45]:

$$k_{rw} = k^*_{rw} S^a \tag{2}$$

$$k_{ro} = k^*_{ro} (1 - S)^b \tag{3}$$

$$S = \frac{S_w - S_{wi}}{1 - S_{or} - S_{wi}} \tag{4}$$

$$p_c = J(S)\sigma\sqrt{\frac{\phi}{k}} \tag{5}$$

where k^*_{rw} is maximum relative permeability of water phase, dimensionless; k^*_{ro} is maximum relative permeability of oil phase, dimensionless; k_{ro} is relative permeability of oil phase, dimensionless; k_{rw} is relative permeability of water phase, dimensionless; a is water phase relative permeability exponent, dimensionless; b is oil phase relative permeability exponent, dimensionless; S is normalized water saturation, dimensionless; S_{wi} is connate water saturation, dimensionless; S_{or} is residual oil saturation, dimensionless; σ is interfacial tension, mN/m; ϕ is reservoir porosity, dimensionless.

The mass conservation equations for oil–water two-phase flow incorporating the osmotic pressure term are as follows:

$$\begin{cases} \nabla\left(\rho_o \frac{k k_{ro}}{\mu_o} \nabla p_o\right) + q_o = \frac{\partial}{\partial t}(\rho_o \phi S_o) \\ \nabla\left(\rho_w \frac{k k_{rw}}{\mu_w} (\nabla p_w - \nabla \pi)\right) + q_w = \frac{\partial}{\partial t}(\rho_w \phi S_w) \end{cases} \tag{6}$$

where p_w is water phase pressure, Pa; p_o is oil phase pressure, Pa; S_w is water saturation, dimensionless; S_o is oil saturation, dimensionless; k is absolute permeability, m^2; t is time, s; ρ_o is oil phase density, kg/m^3; ρ_w is water phase density, kg/m^3.

Let q_v denote the total flow rate of oil and water, such that q_v is defined as $q_v = q_{wv} + q_{ov}$; λ_o and λ_w represent the mobility coefficients of the oil and water phases, respectively:

$$\lambda_o = \frac{k k_{ro}}{\mu_o}, \ \lambda_w = \frac{k k_{rw}}{\mu_w} \tag{7}$$

where μ_o is viscosity of non-wetting phase fluid, Pa·s; μ_w is viscosity of wetting phase fluid, Pa·s.

Let λ denote the total mobility, such that $\lambda = \lambda_o + \lambda_w$. The capillary pressure is introduced as $p_o = p_c + p_w$.

Assume that the block-centered grid shown in Figure 2 is adopted, with uniform grid sizes (i.e., $\Delta x = \Delta y$), and that a well is located at the center of the grid block to perform the injection–soaking–production cycle. The capillary pressure and osmotic pressure are evaluated using the values from the previous time step.

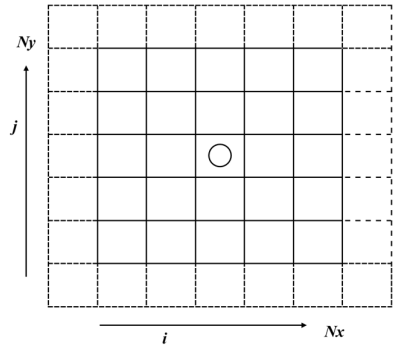


Figure 2. Schematic of grid discretization.

The coefficient matrix for the pressure solution is then given as follows. Taking the grid block (i, j) as the center, the transmissibility between it and its four adjacent grid blocks is defined as:

$$\begin{cases} T_{i+\frac{1}{2},j} = \frac{2\lambda_{i,j}\lambda_{i+1,j}}{\lambda_{i,j}+\lambda_{i+1,j}} \cdot \frac{1}{\Delta x^2} \\ T_{i-\frac{1}{2},j} = \frac{2\lambda_{i-1,j}\lambda_{i,j}}{\lambda_{i-1,j}+\lambda_{i,j}} \cdot \frac{1}{\Delta x^2} \\ T_{i,j+\frac{1}{2}} = \frac{2\lambda_{i,j}\lambda_{i,j+1}}{\lambda_{i,j}+\lambda_{i,j+1}} \cdot \frac{1}{\Delta y^2} \\ T_{i,j-\frac{1}{2}} = \frac{2\lambda_{i,j-1}\lambda_{i,j}}{\lambda_{i,j-1}+\lambda_{i,j}} \cdot \frac{1}{\Delta y^2} \end{cases} \tag{8}$$

$$\sum T = T_{i+\frac{1}{2},j} + T_{i-\frac{1}{2},j} + T_{i,j+\frac{1}{2}} + T_{i,j-\frac{1}{2}} \tag{9}$$

The constructed matrix corresponds to the left-hand-side coefficients, and the right-hand-side terms are calculated as follows.

$$RHS_{i,j} = q_{i,j} - (\nabla \cdot (\lambda_o \nabla p_c))_{i,j} + (\nabla \cdot (\lambda_w \nabla \pi))_{i,j} \tag{10}$$

$$\begin{aligned} (\nabla \cdot (\lambda_o \nabla p_c))_{i,j} = {} & \frac{1}{\Delta x}\left(\lambda_{o,i+\frac{1}{2},j}\frac{p_{c,i+1,j}-p_{c,i,j}}{\Delta x} - \lambda_{o,i-\frac{1}{2},j}\frac{p_{c,i,j}-p_{c,i-1,j}}{\Delta x}\right) \\ & + \frac{1}{\Delta y}\left(\lambda_{o,i,j+\frac{1}{2}}\frac{p_{c,i,j+1}-p_{c,i,j}}{\Delta y} - \lambda_{o,i,j-\frac{1}{2}}\frac{p_{c,i,j}-p_{c,i,j-1}}{\Delta y}\right) \end{aligned} \tag{11}$$

$$\begin{aligned} (\nabla \cdot (\lambda_w \nabla \pi))_{i,j} = {} & \frac{1}{\Delta x}\left(\lambda_{w,i+\frac{1}{2},j}\frac{\pi_{i+1,j}-\pi_{i,j}}{\Delta x} - \lambda_{w,i-\frac{1}{2},j}\frac{\pi_{i,j}-\pi_{i-1,j}}{\Delta x}\right) \\ & + \frac{1}{\Delta y}\left(\lambda_{w,i,j+\frac{1}{2}}\frac{\pi_{i,j+1}-\pi_{i,j}}{\Delta y} - \lambda_{w,i,j-\frac{1}{2}}\frac{\pi_{i,j}-\pi_{i,j-1}}{\Delta y}\right) \end{aligned} \tag{12}$$

The term q_{vi} in the finite difference equation is discussed for three distinct stages in a single huff-and-puff cycle:

(1) Injection stage: The source/sink term in the finite difference equation is set as $q_{vi} = q_v$, and the transmissibility coefficients are evaluated using the harmonic averaging principle. (2) Shut-in stage: The source/sink term $q_{vi} = 0$. The pressure distribution in the grid is governed primarily by capillary pressure and osmotic pressure effects. The transmissibility coefficients are still evaluated using the harmonic averaging principle. (3) Production stage: The central well is operated at a constant rate for production.

Based on the water saturation seepage equation (Equation (8)), the explicit update formula for water saturation is derived as:

$$S_{\mathrm{w}}^{n+1} = S_{\mathrm{w}}^{n} - \frac{\Delta t}{\phi}(\nabla \cdot u_{\mathrm{w}})^{n} - \frac{\Delta t}{\phi} q_{\mathrm{w}}^{n} \tag{13}$$

where the divergence term is discretized over the grid as:

$$(\nabla \cdot u_{\mathrm{w}})_{i,j} = \frac{u_{\mathrm{w},x,i+1/2,j} - u_{\mathrm{w},x,i-1/2,j}}{\Delta x} + \frac{u_{\mathrm{w},y,i,j+1/2} - u_{\mathrm{w},y,i,j-1/2}}{\Delta y} \tag{14}$$

In this way, the water saturation in each grid block can be determined, with the mobility evaluated using the upstream value. Based on the water saturation at each grid block obtained at time step $n+1$, the water activity at each grid block at time step $n+1$ can then be calculated.

Based on Raoult's law, for an ideal solution, the vapor pressure of the solvent p_{g} is related to its mole fraction c_{w} by $p_{\mathrm{g}} = p_{\mathrm{g}}^{*} \cdot c_{\mathrm{w}}$, where p_{g}^{*} denotes the vapor pressure of the pure solvent. To account for the non-ideal behavior of real solutions, the activity a_{w} is introduced and defined as $a_{\mathrm{w}} = p_{\mathrm{g}}/p_{\mathrm{g}}^{*}$. For ideal solutions or sufficiently dilute real solutions, the activity coefficient of the solvent $\gamma \to 1$, leading to $a_{\mathrm{w}} \approx c_{\mathrm{w}}$. A dilute aqueous solution is generally approximated when the mole fraction of the solvent (water) satisfies $c_{\mathrm{w}} \geq 0.99$. Considering the osmotic pressure effect in low-salinity waterflooding, all solutions in this experiment are approximated as dilute solutions. Therefore, only the mole fraction of water at different grid locations needs to be calculated.

When calculating the mole fraction of water, it is necessary to consider not only the number of solute molecules, but rather the number of all solute particles in the solution, because the mole fraction of water is defined as:

$$c_{\mathrm{w}} = \frac{n_{\mathrm{w}}}{n_{\mathrm{w}} + n_{\mathrm{s}}} \tag{15}$$

where c_{w} is mole fraction of water, %; n_{w} is amount of water substance, mol; n_{s} is total amount of all solute particles in solution, mol.

For a strong electrolyte such as NaCl, each NaCl molecule dissociates almost completely into Na^{+} and Cl^{-} in water, with one NaCl molecule contributing two solute particles. Therefore, the effective number of moles of solute particles should equal the number of moles of NaCl multiplied by the dissociation factor i, so as to correctly reflect the actual influence of solute particles on the mole fraction of the solvent.

If the number of moles of NaCl is used directly without multiplying by the van't Hoff factor i, the total number of solute particles will be underestimated, resulting in an overestimated mole fraction of water and consequently an underestimated calculated osmotic pressure. In the colligative property equations, it is the particle concentration, not the molecular concentration, that is employed.

3. Numerical Benchmark Test

To validate the flow behavior in the proposed model, a one-dimensional model without osmotic pressure was compared with simulation results from the commercial software Eclipse using the same parameters. The solid lines represent the Eclipse simulation results, and the hollow squares denote the simulation results of the present model. As shown in Figure 3, Eclipse was used to simulate the water saturation profiles at different times under the same parameters. We selected the results at t = 15, 35, 55, and 100 from the Eclipse simulations for comparison with the proposed model. As illustrated, the results from the present model match well with those from the commercial software. The validation results

demonstrate that the model developed in this study is practical and accurate in predicting flow behavior and characterizing osmotic pressure.

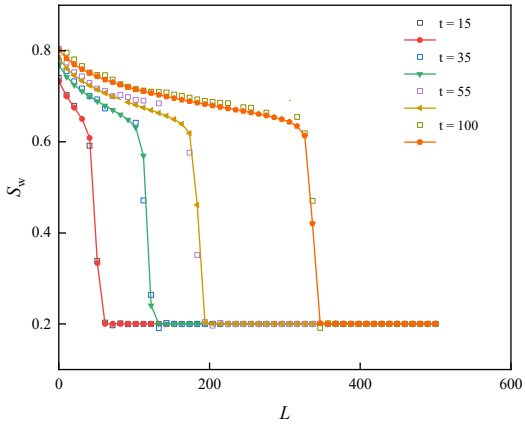


Figure 3. Comparison curves of the proposed model and the commercial software model under identical parameters.

4. Parameter Sensitivity Analysis

To further verify the parameter effects, a base model with a central well in a homogeneous reservoir was first constructed, as shown in Figure 4, with detailed parameters listed in Table 1. A control-variable approach was employed to analyze the influences of injected fluid salinity, soaking time, and injection rate on the huff-and-puff process. The spatial distributions of water saturation, pore pressure, and salt mass fraction, together with the cumulative recovery factor, were obtained under various parameter conditions. The results are presented as follows.

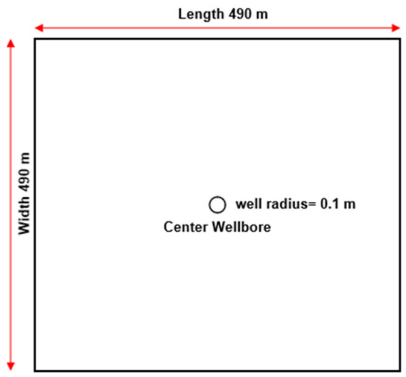


Figure 4. Schematic of the open-hole well physical model.

Table 1. Physical parameters for the simulation.

Parameter Type	Parameter Values
Reservoir porosity ϕ	6.9%
Absolute permeability k	0.052 mD
Non-wetting phase fluid viscosity μ_o	10 mPa·s
Wetting phase fluid viscosity μ_w	1 mPa·s
Initial formation pressure P_0	25 MPa
Rock compressibility	6.6×10^{-10} MPa^{-1}
Oil compressibility	1.0×10^{-4} MPa^{-1}
Water compressibility	1.0×10^{-4} MPa^{-1}
Oil phase density ρ_o	800 kg/m^3

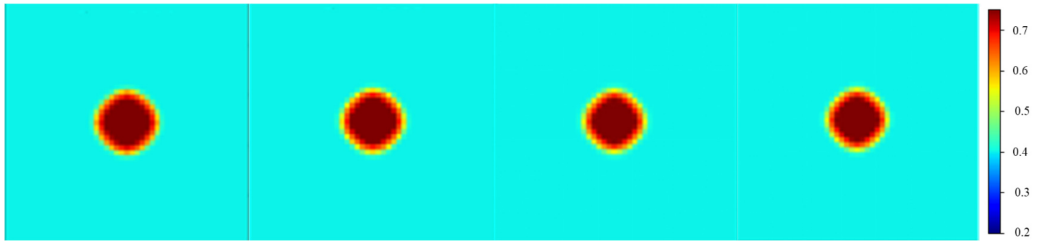
Table 1. *Cont.*

Parameter Type	Parameter Values
Water phase density ρ_w	1000 kg/m^3
Formation water salinity	150,000 mg/L
Irreducible water saturation S_{wi}	0.2
Residual oil saturation S_{or}	0.2
Temperature T_{res}	350 K
constant term R	0.00831 MPa·L/(K·mol)
NaCl dissociation factor i	2.0
constant-rate	8 m^3/d

4.1. Injected-Water Salinity

To reveal the effect of injected-water salinity on huff-and-puff development performance, simulation studies were conducted under different injected-water salinities while keeping all other parameters consistent. The simulation design was as follows: the total injection volume per cycle was fixed at 4800 m^3, the soaking time was 40 d, the injection rate was set at 80 m^3/d, and the injected-water salinity was varied from 1000 mg/L to 50,000 mg/L. Because injected-water salinity significantly affects seepage field evolution, contour maps of water saturation, pore pressure, and salt mass fraction distribution for a single huff-and-puff cycle were specifically plotted to analyze the governing effect of injected-water salinity on pressure propagation, water-swept area, and salt ion migration.

Figure 5 presents the water saturation distributions during the injection stage under different salinity conditions. During the injection stage, the salinity difference exerts little influence on the water saturation front. The primary reason is that the injection pressure differential serves as the absolutely dominant driving force in this stage, whereas the osmotic pressure induced by the low-salinity water is considerably smaller in terms of magnitude, time scale, and spatial extent of influence compared with the dominant force, thus producing no observable effect on the macroscopic water saturation distribution. Consequently, the water saturation contours for the four salinity cases are essentially identical.

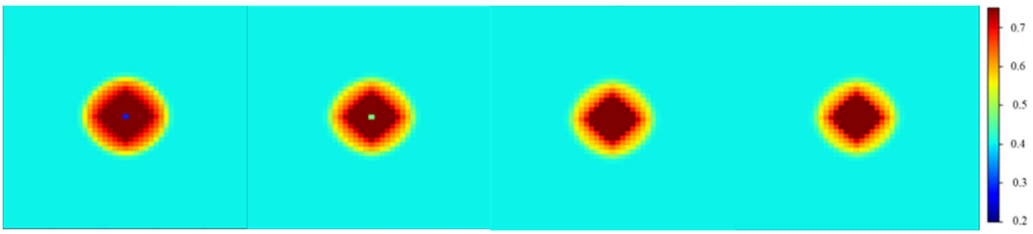


(**a**) 1000 mg/L (**b**) 5000 mg/L (**c**) 20,000 mg/L (**d**) 50,000 mg/L

Figure 5. Water saturation distribution during the injection stage under different salinity conditions.

As shown in Figure 6, compared with the injection stage, the water saturation distributions exhibit significant differences, displaying a gradient pattern in which lower injected-water salinity leads to more pronounced sweep and diffusion of water saturation. Specifically, the 1000 mg/L low-salinity group exhibits the largest water saturation swept radius and the widest water saturation transition zone. In the near-wellbore high-water-saturation core zone, distinct fluid redistribution and a decline in water saturation are observed, realizing a uniform diffusion of water saturation from the near-wellbore region toward the far-field formation. The underlying mechanism is that after shut-in for soaking, in the absence of injection and production, the macroscopic convection that absolutely dominated the injection stage vanishes entirely. Consequently, the previously suppressed effects of low-salinity osmotic pressure, capillary imbibition, and wettability reversal be-

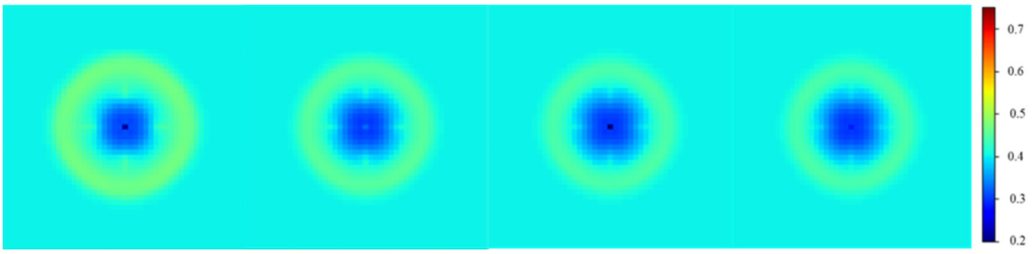
come the dominant forces governing fluid migration. Quantitatively, under the 1000 mg/L injected-water salinity condition, the osmotic pressure calculated by Equation (1) is approximately 3.9 MPa, while the capillary pressure ranges from 2.0 to 5.0 MPa depending on water saturation, and the viscous pressure drop during injection is on the order of several MPa. During the soaking stage, forced convection ceases and the viscous pressure drop essentially vanishes; therefore, capillary pressure remains the dominant driving force, whereas osmotic pressure, though generally lower than capillary pressure, is of the same order of magnitude and plays a key role alongside capillary pressure in promoting spontaneous imbibition and fluid redistribution. A larger ionic concentration difference between the injected water and the original formation water induces a stronger osmotic-pressure driving effect, which more effectively pushes water saturation into previously unswept oil-bearing pores. This result also directly demonstrates that the soaking stage is the core phase through which low-salinity water huff-and-puff achieves enhanced oil recovery and efficiency.



(**a**) 1000 mg/L (**b**) 5000 mg/L (**c**) 20,000 mg/L (**d**) 50,000 mg/L

Figure 6. Water saturation maps during the soaking stage under different salinity conditions.

As shown in Figure 7, the driving pressure differential during the production stage is significantly lower than that during the injection stage, and the fluid seepage velocity decreases substantially. Nevertheless, the osmotic pressure and capillary force induced by the low-salinity water can continue to act. In the hydrophilic formation resulting from wettability reversal, capillary force and osmotic pressure displace crude oil from the pores while retaining the water phase in the far-field pores, thereby preventing it from being rapidly produced. Consequently, a higher water saturation is preserved in the far-wellbore region. As illustrated in the figure, under the condition of 1000 mg/L salinity, the retained water saturation in the far-wellbore area is represented by a deeper yellow color.



(**a**) 1000 mg/L (**b**) 5000 mg/L (**c**) 20,000 mg/L (**d**) 50,000 mg/L

Figure 7. Water saturation maps during the production stage under different salinity conditions.

Figure 8 presents the pore pressure profiles in the near-wellbore region during the injection stage under different salinity conditions. Macroscopically, varying the injected-water salinity has virtually no effect on pore pressure because the imposed pressure gradient of the injected water is sufficiently large. Microscopically, however, at a given location, a smaller salinity difference between the injected water and the formation water leads to a

slightly higher oil-phase pressure, whereas a larger salinity difference results in a slightly lower oil-phase pressure.

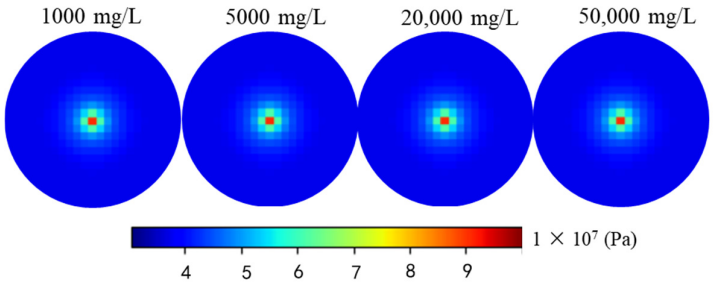


Figure 8. Pore pressure maps in the near-wellbore region during the injection stage under different salinity conditions.

As can be seen from Figure 9, the overall trend is that a lower injected-water salinity—hence a larger salinity difference with the original formation water—results in more sufficient pressure diffusion during the soaking stage, better uniformity of the global pore pressure field, and more significant energy replenishment in the far-field region. Once the pore pressure has fully diffused, the average pore pressure shows almost no difference.

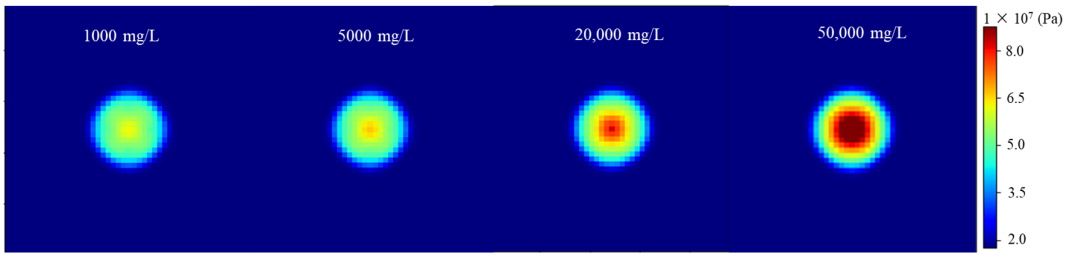


Figure 9. Pore pressure maps in the near-wellbore region during the soaking stage under different salinity conditions.

Figure 10 displays the contour maps of the pore pressure distribution in the near-wellbore region during the production stage under different salinity conditions, directly illustrating the spatial distribution characteristics and variation patterns of formation pore pressure for the four systems: 1000 mg/L, 5000 mg/L, 20,000 mg/L, and 50,000 mg/L. In terms of the overall morphology of the pore pressure field, the pore pressure fields in the production stage under all salinity conditions exhibit a typical pressure-drop-funnel distribution: in the near-wellbore region centered on the wellbore, pore pressure drops rapidly due to continuous fluid withdrawal, forming a distinct low-pressure zone; in the reservoir periphery far from the wellbore, pore pressure remains at a relatively high level. The pore pressure decreases stepwise from the far field toward the wellbore, which is an inevitable consequence of fluid flow toward the wellbore during production. A comparison of the pore pressure fields under different salinity conditions reveals that, despite the significant differences in injected-water salinity, there is no noticeable difference in the distribution pattern of pore pressure or in the extent and steepness of the pressure-drop funnel among the various systems. This indicates that during the production stage at a constant withdrawal rate, salinity exerts a weak influence on the overall distribution characteristics of the pore pressure field, and that the dominant factor controlling the pore pressure gradient remains the withdrawal rate rather than the injected-water salinity.

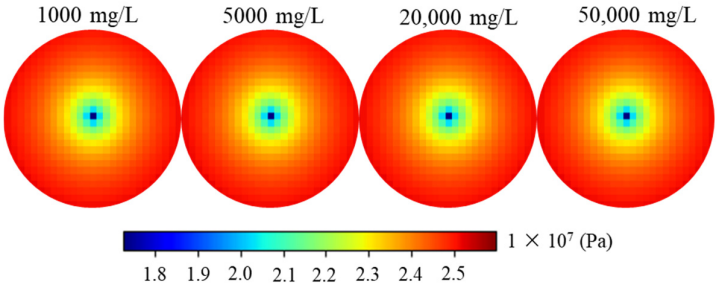
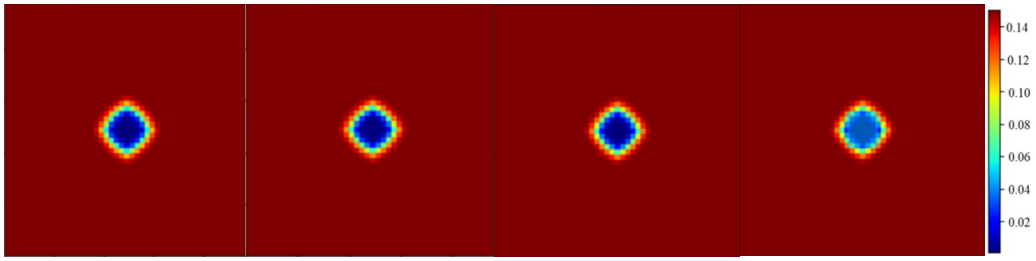


Figure 10. Pore pressure maps in the near-wellbore region during the production stage under different salinity conditions.

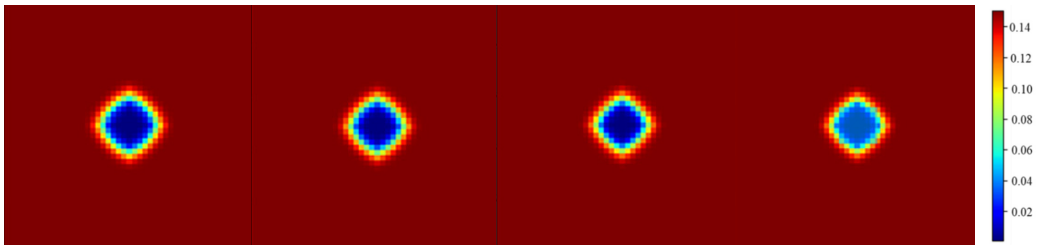
As with the water saturation distributions in Figure 5, the salt mass fraction distributions during the injection stage (Figure 11) for different salinities are virtually identical in terms of distribution pattern, swept area, and gradient variation, exhibiting no significant differences. All display a radially symmetric distribution centered on the injection well, with a low-salinity core near the wellbore that transitions outward in a ring-like gradient to the high-salinity background of the original formation water in the far-field region. The only difference is that the color of the injected-water core in the contour map is determined by the salinity of the injected water.



(**a**) 1000 mg/L (**b**) 5000 mg/L (**c**) 20,000 mg/L (**d**) 50,000 mg/L

Figure 11. Salt mass fraction maps during the injection stage under different salinity conditions.

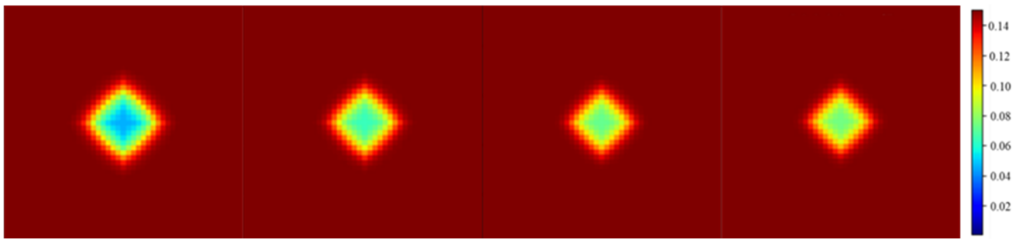
Figure 12 presents the salt mass fraction distributions during the soaking stage under different salinity conditions. During the soaking stage, capillary pressure and osmotic pressure are the primary driving mechanisms, where the magnitude of osmotic pressure is determined by the salinity difference between the formation water and the injected water. Salt gradually approaches equilibrium distribution within the pores, further constraining the extent of mass fraction changes. Compared with the injection stage (Figure 11), all four sub-figures in Figure 12 exhibit varying degrees of diffusion. Among them, the 1000 mg/L case shows a larger extent of diffusion, with a wider and more distinct mixing boundary between the formation water and the injected water.



(**a**) 1000 mg/L (**b**) 5000 mg/L (**c**) 20,000 mg/L (**d**) 50,000 mg/L

Figure 12. Salt mass fraction maps during the soaking stage under different salinity conditions.

Figure 13 shows the salt mass fraction distributions during the production stage under different salinity conditions. In the production stage, the low-salinity injected water near the wellbore is preferentially produced, while the high-salinity formation water in the far-field region flows toward the wellbore under the pressure gradient to replenish the withdrawn fluid. These two fluids undergo convective mixing, causing the salt mass fraction near the wellbore to increase significantly compared with the soaking stage, thereby forming a salt mass fraction transition zone centered on the wellbore. The physical essence of this phenomenon is that convection dominates the production stage: the production rate and pressure gradient drive large-scale fluid flow and mixing, masking the effect of molecular diffusion. Consequently, the initial injected-water salinity directly determines the lower limit of the salt mass fraction in the near-wellbore region after mixing.



(**a**) 1000 mg/L (**b**) 5000 mg/L (**c**) 20,000 mg/L (**d**) 50,000 mg/L

Figure 13. Salt mass fraction maps during the production stage under different salinity conditions.

The salinity difference between the injected water and the formation water serves as the driving force for enhanced oil recovery in low-salinity water huff-and-puff; the greater the salinity difference, the stronger the resulting osmotic pressure gradient. During the injection stage, the direction of osmotic pressure driving is from the wellbore toward the deeper reservoir, inducing spontaneous imbibition of water saturation into oil-bearing pores and displacing the crude oil, thereby improving the oil recovery efficiency. During the soaking stage, the osmotic pressure difference driven by the concentration gradient further promotes the preferential entry of water saturation into small pores or oil-wet pores in tight reservoirs, achieving deep displacement of residual oil. During the production stage, the displaced oil is produced along with the fluid flow, ultimately realizing an enhancement in oil recovery. According to the simulation results presented in Table 2, the traditional huff-and-puff method, represented by high-salinity injection water (50,000 mg/L), yields a recovery factor of 8.42%. When the injected-water salinity is reduced to 1000 mg/L, the recovery factor increases to 10.94%, corresponding to an incremental recovery of 2.52 percentage points (approximately 29.9% relative improvement). This demonstrates the most significant oil-increment effect and is identified as the optimal injected-water salinity for single-cycle low-salinity water huff-and-puff in this tight oil reservoir.

Table 2. Oil recovery under different salinity conditions.

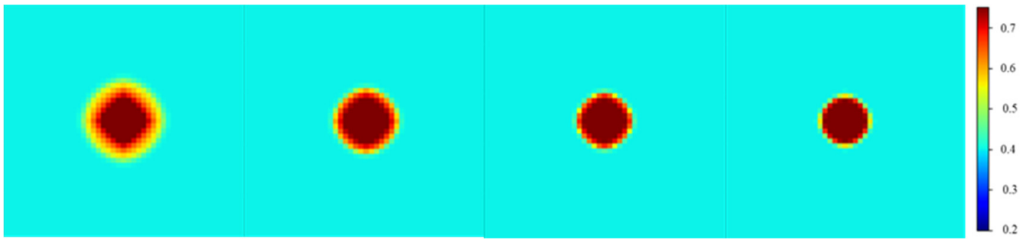
No.	Huff-and-Puff Cycle	Salinity (mg/L)	Cumulative Oil Production (m^3)	Recovery Factor (%)
1	1	1000	8699.6105	10.94
2	1	5000	7928.2556	9.97
3	1	20,000	6942.1937	8.73
4	1	50,000	6695.6783	8.42

4.2. Injection Rate

To reveal the effect of injection rate on the development performance of low-salinity water huff-and-puff, simulation studies were conducted under different injection rates

while keeping all other parameters consistent. The simulation design was as follows: the total injection volume per cycle was fixed at 4800 m^3, the soaking time was 40 d, and the injection rate was varied from 40 to 160 m^3/d. Because the injection rate significantly influences seepage field evolution during the injection stage, contour maps of water saturation, pore pressure, and salt mass fraction distribution for a single huff-and-puff cycle were specifically plotted to analyze the governing effect of injection rate on pressure propagation, water-swept area, and salt ion migration.

Figure 14 presents the water saturation contour maps during the injection stage at different injection rates. As can be observed from the saturation field characteristics, when the total injection volume per cycle is fixed, the extent of the high-water-saturation zone near the wellbore first undergoes slight variation and then shrinks significantly as the injection rate increases, rather than expanding monotonically. The overall swept volume decreases markedly under high-rate conditions. The high flow rate prevents the injected water from having sufficient time to sweep the formation, ultimately resulting in a contraction of the water saturation distribution when the injection rate becomes excessively high. This change in the swept area directly affects subsequent development performance: an excessively low injection rate yields a large swept area but prolongs the development cycle, whereas an excessively high injection rate generates a large injection pressure gradient in the short term, but water channeling and viscous fingering reduce the swept volume. Therefore, an optimal injection rate interval exists, within which adequate displacement pressure can be ensured while shortening the injection period.

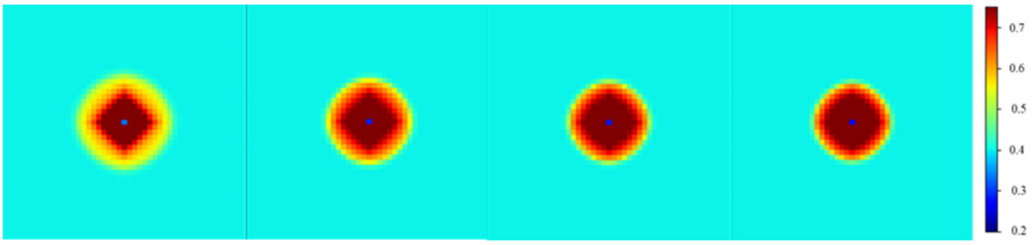


(**a**) 40 m^3/d (**b**) 80 m^3/d (**c**) 120 m^3/d (**d**) 160 m^3/d

Figure 14. Water saturation maps during the injection stage under different injection rates.

Figure 15 shows the water saturation contour maps during the soaking stage under different injection rates. From the perspective of displacement mechanisms, injection operations cease during the soaking stage, and the forced convection of water saturation vanishes. Instead, under the combined action of capillary force and molecular diffusion, slow imbibition and diffusion occur toward the low-water-saturation regions that were unswept during the injection stage, driving the saturation field from a heterogeneous distribution toward homogenization. At this stage, the injection rate is no longer a direct controlling factor for water saturation migration; the redistribution of water saturation during the soaking process is entirely determined by the initial water saturation field established during the preceding injection stage. A comparison of the water saturation fields under different injection rates reveals that after soaking, the diffusion extent and distribution pattern of water saturation are highly correlated with the effectively swept area during the injection stage. When the injection rate during the injection stage falls within a reasonable range, the waterflood sweep efficiency is high, the resulting initial water saturation field is more uniform, and the scope for capillary imbibition and diffusion during soaking is larger, leading to a more sufficient redistribution effect. Conversely, if the injection rate is excessively high, causing water channeling and fingering, the effectively swept area during injection is limited, and the water saturation redistribution during soaking can only proceed within the limited initial saturation zone, unable to overcome

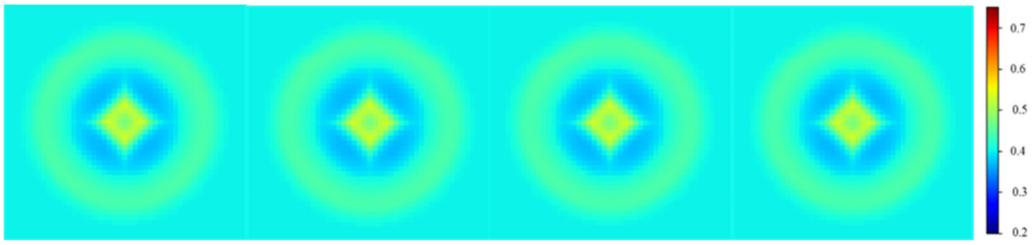
the heterogeneity inherited from the previous stage. Therefore, when the total injection volume per cycle is fixed, the differences in water saturation diffusion during the soaking stage at different injection rates are essentially a continuation of the influence of injection rate on sweep efficiency in the injection stage, rather than a direct result of the injection rate during the soaking process.



(**a**) 40 m³/d (**b**) 80 m³/d (**c**) 120 m³/d (**d**) 160 m³/d

Figure 15. Water saturation maps during the soaking stage under different injection rates.

Figure 16 displays the water saturation contour maps during the production stage under different injection rates, visually illustrating the influence of injection rate on the water saturation field at the early production stage and also reflecting the chain effects of the preceding injection and soaking stages. Regarding the overall distribution pattern of the saturation field, after the well is opened for production, formation fluids flow toward the wellbore under the pressure gradient. The water saturation field exhibits a typical distribution characteristic of "high in the wellbore center and low in the far-field region": a high-water-saturation zone is formed around the wellbore, gradually transitioning outward to a moderate-saturation transition zone and a low-saturation zone, with distinct annular transition structures present under all injection rate conditions. A comparison of the saturation fields under the four injection rates reveals that when the total injection volume per cycle is fixed, within the range of injection rates investigated in this study, the differences in the water saturation field at the early production stage among different injection rates are not significant.



(**a**) 40 m³/d (**b**) 80 m³/d (**c**) 120 m³/d (**d**) 160 m³/d

Figure 16. Water saturation maps during the production stage under different injection rates.

From Figure 17, it can be observed during the injection stage that the high pore pressure zone is tightly confined around the wellbore and rapidly decays outward into a blue low-pressure zone. As the injection rate increases, the high-pressure influence radius expands slightly, but the pore pressure in the core zone rises much faster. This indicates that, under the current injection rates, the formation absorption capacity is insufficient and the energy transfer efficiency is low. In tight reservoirs, excessively high injection rates cause the near-wellbore pore pressure to build up rapidly; therefore, the injection rate should not be set too high, as this may easily cause the wellbore pressure to exceed the formation fracturing pressure.

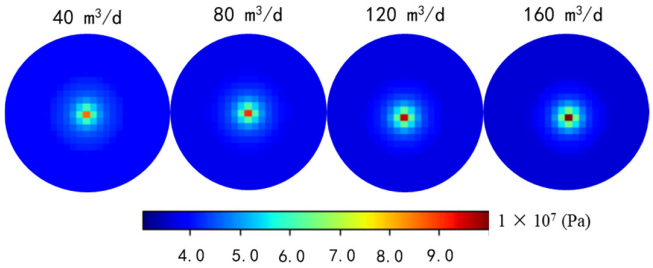


Figure 17. Pore pressure maps in the near-wellbore region during the injection stage under different injection rates.

Figure 18 demonstrates that, compared with the injection stage, the formation pore pressure during the soaking stage is significantly elevated overall. The lower the injection rate, the higher the average post-soaking formation pore pressure and the larger the high-pressure swept area. Given the low-permeability characteristics of tight reservoirs, a low injection rate promotes the diffusion of low-salinity water into the deep matrix, fully leveraging ion exchange and wettability reversal effects, thereby enhancing energy retention. In contrast, a high injection rate tends to induce near-wellbore channeling and energy dissipation, reducing the average formation pore pressure. Therefore, the optimal injection rate range for low-salinity water huff-and-puff in tight oil reservoirs is 40–80 m^3/d.

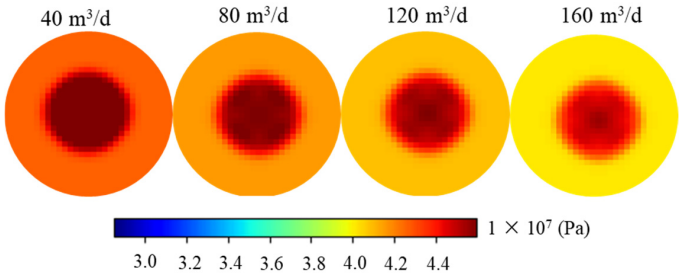


Figure 18. Pore pressure maps in the near-wellbore region during the soaking stage under different injection rates.

Figure 19 presents the pore pressure profiles in the near-wellbore region during the production stage under different injection rates. At the end of a prolonged production period, the pore pressures are essentially identical across cases. However, at the early stage of production, the pore pressure decline under low-rate injection is global in nature: the injected energy is uniformly stored throughout the reservoir, and during production, it can mobilize matrix flow over a larger area. When the injection rate is excessively high, a high-pressure core forms near the wellbore, but the pressure fails to propagate to the boundaries. From the production stage perspective, the lower the injection rate, the better the pore pressure diffusion.

As can be seen from Figure 20, when the injection rate increases from 40 m^3/d to 160 m^3/d, the higher the injection rate, the smaller the fluid swept area. This is attributed to the nature of tight reservoirs; an excessively high injection rate reduces the swept area during the injection process, resulting in a decrease in cumulative oil production.

Figure 21 shows the contour maps of salt mass fraction distribution during the soaking stage under different injection rates, intuitively reflecting the effect of injection rate on the redistribution of the salt mass fraction field. During the soaking stage, injection ceases, and osmotic pressure and capillary pressure become dominant, driving water from low-salinity regions to high-salinity regions and causing the salt mass fraction field to gradually diffuse. As the injection rate increases, the central low-salinity zone exhibits a clear shrinking trend,

which is highly consistent with the variation pattern of the water saturation field. This difference is not a direct consequence of the injection rate during the soaking stage, but rather a continuation of the influence of injection rate on waterflood sweep efficiency during the injection stage. The lower the injection rate, the wider the effective swept area formed during injection, and consequently, the more complete the homogenization of the salt mass fraction field after soaking.

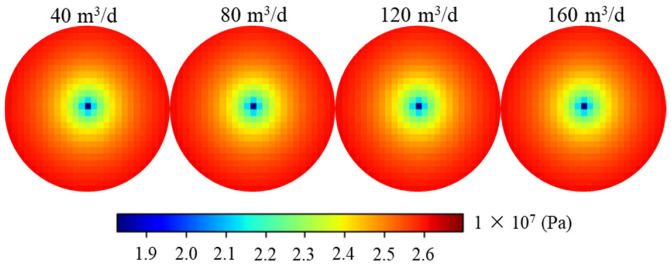
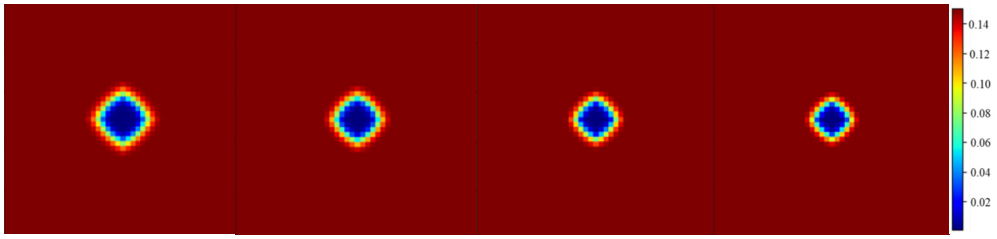
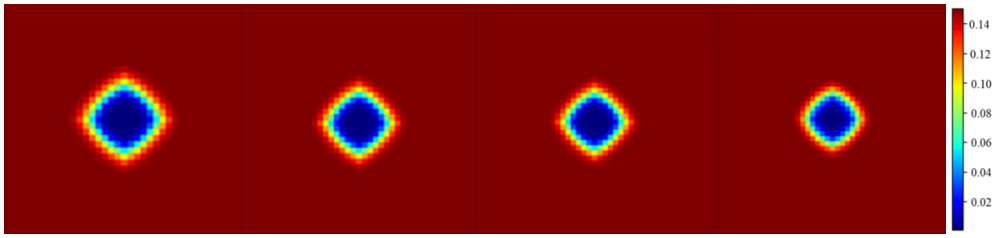


Figure 19. Pore pressure maps in the near-wellbore region during the production stage under different injection rates.



(**a**) 40 m³/d (**b**) 80 m³/d (**c**) 120 m³/d (**d**) 160 m³/d

Figure 20. Salt mass fraction distribution maps during the injection stage under different injection rates.

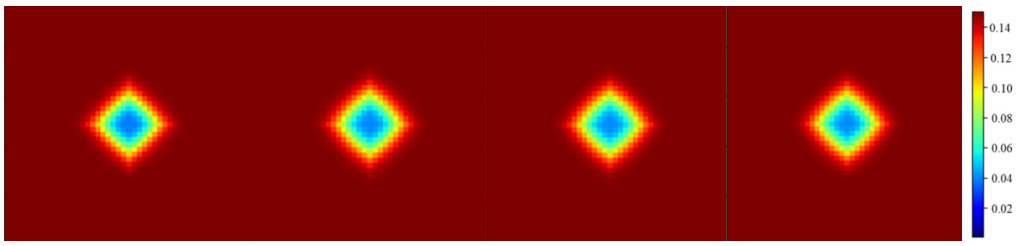


(**a**) 40 m³/d (**b**) 80 m³/d (**c**) 120 m³/d (**d**) 160 m³/d

Figure 21. Salt mass fraction distribution maps during the soaking stage under different injection rates.

Figure 22 presents the contour maps of salt mass fraction distribution during the production stage under different injection rates, intuitively illustrating the influence of injection rate on the salt mass fraction field during the production process. After the well is opened for production, the low-salinity injected water near the wellbore is preferentially produced, while the high-salinity formation water in the far field flows toward the wellbore under the pressure gradient to supplement the produced fluids, causing an overall increase in the near-wellbore salt mass fraction. Under different injection rates, the differences in the near-wellbore salt mass fraction field are relatively small, all exhibiting a pattern of slightly lower values in the center and higher values in the periphery. This phenomenon indicates that the salt mass fraction field at the early production stage is primarily governed by the mixed state established after soaking, and the direct influence of injection rate is weakened. The differences introduced by injection rate are more prominently reflected

in the subsequent water-cut rise dynamics rather than in the initial salt mass fraction distribution itself.



(**a**) 40 m³/d (**b**) 80 m³/d (**c**) 120 m³/d (**d**) 160 m³/d

Figure 22. Salt mass fraction distribution maps during the production stage under different injection rates.

As can be seen from the simulation results in Table 3, during the first huff-and-puff cycle, the injection rate has a significant effect on the production performance. As the injection rate gradually increases from 40 m^3/d to 160 m^3/d, both cumulative oil production and recovery factor exhibit a continuous decreasing trend. Specifically, at an injection rate of 40 m^3/d, the cumulative oil production reaches 8850.70 m^3, with a recovery factor of 11.13%, which is the highest among all cases. When the injection rate is increased to 80 m^3/d, the cumulative oil production is 8699.61 m^3 and the recovery factor is 10.94%, only a slight decrease of 0.19 percentage points compared with the 40 m^3/d case. As the injection rate is further raised to 120 m^3/d and 160 m^3/d, the recovery factors drop to 10.32% and 9.78%, respectively, indicating a marked deterioration in development performance. From the perspective of flow mechanisms, this pattern is fully consistent with the seepage characteristics of tight oil reservoirs: when the injection rate is excessively high, very little injected water imbibes into the matrix pores, making it difficult to displace oil through imbibition, which significantly reduces both sweep efficiency and displacement efficiency and ultimately leads to a notable decline in recovery factor. Conversely, a relatively low injection rate ensures sufficient contact between injected water and the matrix and maximizes the imbibition effect to achieve a higher recovery factor. However, an excessively low injection rate would result in an overly long injection period, substantially increasing operational and time costs and reducing the economic viability of field development. If the sole objective is to maximize ultimate recovery without regard to time or cost, 40 m^3/d would be the optimal choice. However, considering that the recovery factor at 80 m^3/d (10.94%) is only 0.19 percentage points lower than that at 40 m^3/d (11.13%), while the injection time required to deliver the same total injection volume per cycle is reduced by half, the 80 m^3/d rate achieves a more favorable balance between oil recovery and development cycle length. Based on the optimization criterion of maximizing recovery per unit time (i.e., balancing incremental oil recovery against operational time), 80 m^3/d is recommended as the preferred injection rate for this tight oil reservoir. The final selection of the injection rate should ultimately depend on the specific economic constraints and development objectives of the field.

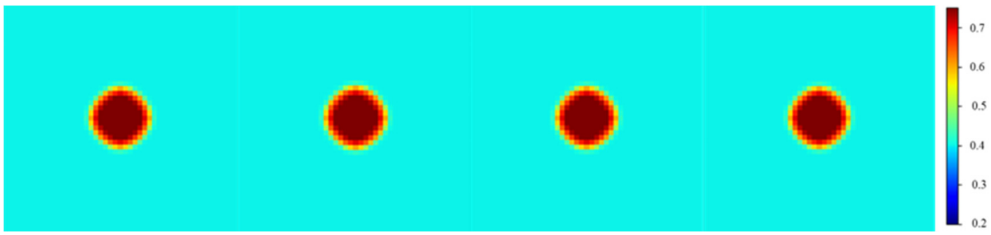
Table 3. Oil recovery under different injection rate conditions.

No.	Huff-and-Puff Cycle	Injection Rate (m^3/d)	Cumulative Oil Production (m^3)	Recovery Factor (%)
1	1	40	8850.70	11.13
2	1	80	8699.61	10.94
3	1	120	8206.57	10.32
4	1	160	7777.16	9.78

4.3. Soaking Time

To reveal the effect of soaking time on the development performance of low-salinity water huff-and-puff, simulation studies were conducted under different soaking times while keeping all other parameters consistent. The simulation design was as follows: the total injection volume per cycle was fixed at 4800 m^3, the soaking time was varied from 20 to 80 d, and the injection rate was set at 80 m^3/d. Contour maps of water saturation, pore pressure, and salt mass fraction distribution for a single huff-and-puff cycle were specifically plotted to analyze the governing effect of soaking time on pressure propagation, water-swept area, and salt ion migration.

Figure 23 presents water saturation distribution maps during the water injection stage under different soaking times, reflecting the influence of the preceding soaking duration on subsequent waterflood performance. From 20 d to 80 d, the morphology of the water saturation field during injection remains highly consistent, with no obvious differences in the extent of the high-saturation zone or the characteristics of the transition zone. This indicates that, under the conditions of this study, soaking time does not affect the water saturation distribution during the injection stage. The sweep efficiency in the injection stage is mainly governed by the investigated injection rate.



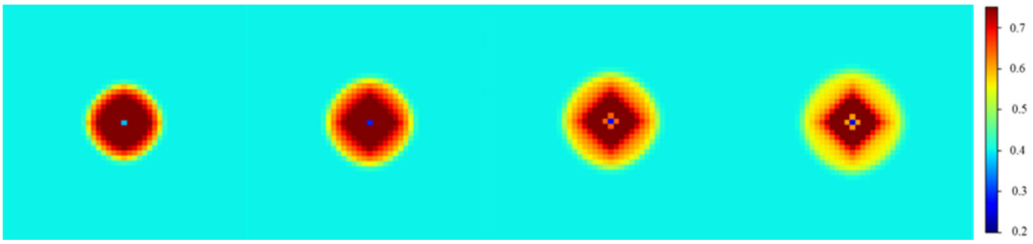
(**a**) 20 d (**b**) 40 d (**c**) 60 d (**d**) 80 d

Figure 23. Water saturation maps during the injection stage under different soaking times.

Figure 24 shows the water saturation distribution maps at different soaking times, directly illustrating the effect of soaking duration on water saturation redistribution. For a soaking time of 20 d, the high-water-saturation zone is confined to the near-wellbore region, with a very limited sweep range. As the soaking time increases to 40 d, the high-saturation zone expands outward, the transition zone broadens noticeably, and water saturation begins to penetrate into the far-well area. At 60 d, the redistribution enters a rapid development stage, and the uniformity of the overall water saturation field improves significantly. By 80 d, the diffusion of water saturation tends to stabilize, and the expansion rate of the high-saturation zone slows down appreciably. This process is dominated by capillary force and osmotic pressure, with water saturation spontaneously imbibing and diffusing into low-saturation pores under no-forced-convection conditions. The period of 20–60 d is the efficient stage for water saturation redistribution; extending soaking time can effectively improve sweep efficiency. After 60 d, the marginal benefit of further redistribution decreases substantially, and excessively long soaking brings no significant gains. A uniform water saturation distribution can reduce the risk of water breakthrough in the subsequent production stage and enhance oil displacement efficiency. Therefore, an optimal soaking-time interval exists, which should be determined by balancing redistribution effectiveness and development cycle time.

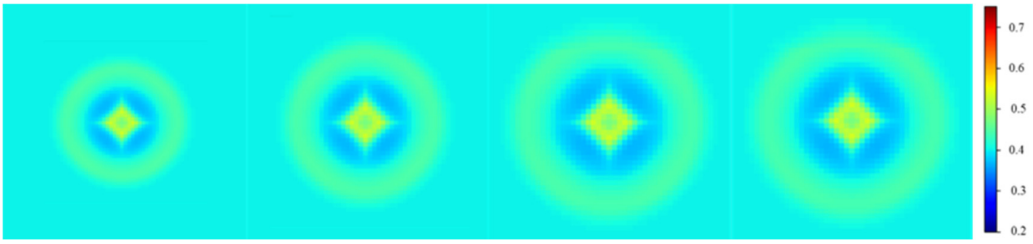
Figure 25 displays the water saturation distribution maps during the production stage under different soaking times, directly reflecting the regulatory effect of soaking time on subsequent water saturation distribution. As the soaking time increases from 20 d to 80 d, the influence range of water saturation expands markedly, and the high-to-moderate saturation annulus gradually extends outward. At 20 d of soaking, water saturation is

mainly concentrated near the wellbore, with a limited radius of influence, and the water saturation in the peripheral reservoir remains relatively low. After 40 d, the distribution range begins to expand outward, and the width of the saturation transition zone increases significantly. At 60–80 d, the swept area of water saturation further enlarges, and the water saturation in the peripheral formation is notably enhanced. This change stems from the redistribution effect during the soaking stage: the longer the soaking time, the more fully the water saturation undergoes imbibition and diffusion driven by capillary and osmotic forces. Adequate soaking results in a more uniform water saturation distribution in the reservoir, forming a broader water saturation influence region for the subsequent production stage. The 20–60 d period is the efficient phase for redistribution; extending soaking time can clearly improve the subsequent sweep efficiency of water saturation. Beyond 60 d, the increment in water saturation distribution diminishes. A reasonable soaking time can optimize the water saturation distribution during production, delay water breakthrough, and enhance oil-phase recovery efficiency.



(**a**) 20 d (**b**) 40 d (**c**) 60 d (**d**) 80 d

Figure 24. Water saturation maps during the soaking stage under different soaking times.



(**a**) 20 d (**b**) 40 d (**c**) 60 d (**d**) 80 d

Figure 25. Water saturation maps during the production stage under different soaking times.

Figure 26 presents the pore pressure distribution in the near-wellbore region during the injection stage under different soaking times. Across the four cases ranging from 20 d to 80 d, the pore pressure fields remain highly consistent in morphology with no noticeable variation, all exhibiting a typical distribution pattern of high pressure in the center and low pressure in the periphery. Neither the extent, gradient, nor peak value of the pore pressure field changes as the soaking time increases. This indicates that soaking time exerts no direct influence on the pore pressure distribution during the injection stage. The pore pressure field in the injection stage is primarily controlled by the injection pressure, injection rate, and reservoir properties. Soaking time is an operational parameter of the soaking stage and does not participate in the establishment of pore pressure during the injection process; hence, the pore pressure distributions under different soaking times remain identical. The pore pressure field is dominated by the forced displacement of the injected fluid and is unrelated to the preceding soaking period.

Figure 27 illustrates the pore pressure distribution characteristics in the near-wellbore region during the soaking stage under different soaking times. As can be observed, the longer the soaking time, the higher the overall pore pressure level in the near-wellbore

region and the more uniform the distribution. At 80 d of soaking, the entire region appears almost deep red, with pore pressure maintained at a high level, indicating that prolonged soaking allows the high-pressure fluid to fully diffuse within the matrix and achieve thorough energy replenishment. As the soaking time decreases, the color in the 60 d and 40 d soaking regions shifts from deep red to orange-red and then to orange, accompanied by a gradual decline in pore pressure. At 20 d of soaking, the periphery already appears bright yellow, with only a small area near the wellbore retaining high pressure, demonstrating that short soaking durations lead to insufficient fluid diffusion and an overall low energy level in the near-wellbore region. Moreover, the longer the soaking time, the gentler the pore pressure gradient between the center and the periphery, and the more uniform the pore pressure field distribution. This favors the formation of a stable displacement driving force in the subsequent production stage and lays the foundation for enhancing oil recovery.

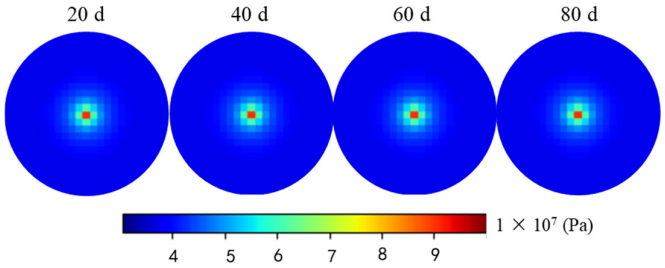


Figure 26. Pore pressure maps in the near-wellbore region during the injection stage under different soaking times.

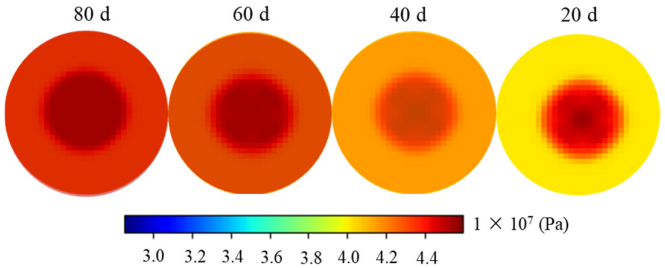


Figure 27. Pore pressure maps in the near-wellbore region during the soaking stage under different soaking times.

Figure 28 shows the pore pressure distribution characteristics in the near-wellbore region of a fractured well during the production stage under different soaking times. At the early production stage, the pore pressure fields exhibit significant differences depending on the soaking time: the shorter the soaking time, the steeper the pore pressure gradient in the near-wellbore region, with the high-pressure zone concentrated around the wellbore and a higher peak pore pressure; the longer the soaking time, the gentler the near-wellbore pore pressure distribution and the more fully the high-pressure zone diffuses toward the far-field region. However, as production progresses, under constant injection and production volumes, the initial differences in pore pressure caused by varying soaking times are gradually eliminated, and the pore pressure distribution in the near-wellbore region eventually becomes consistent. This phenomenon arises from the dynamic equilibrium of the injection–production system energy, indicating that soaking time only affects the pore pressure response characteristics at the early production stage, whereas during the stabilized development stage, the constant injection–production schedule dominates the final distribution pattern of the pore pressure field.

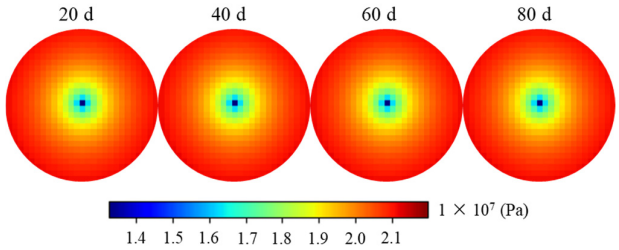
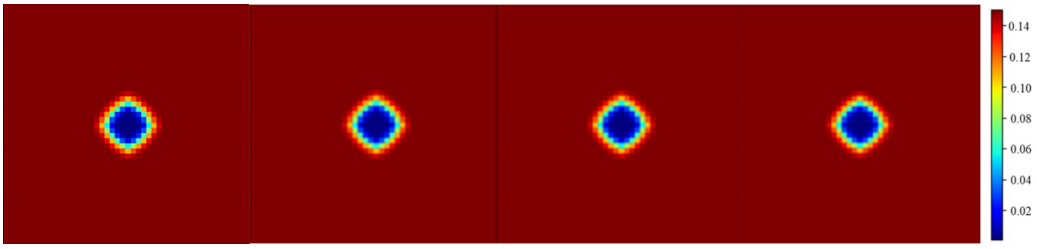


Figure 28. Pore pressure maps in the near-wellbore region during the production stage under different soaking times.

Figure 29 presents the contour maps of salt mass fraction distribution during the injection stage under different soaking times, intuitively illustrating the influence of soaking time on the salt mass fraction field in the injection stage. From 20 d to 80 d, the salt mass fraction distributions under the four cases show virtually no noticeable variation: the extent, morphology, and transition zone characteristics of the central low-salinity region remain highly consistent and exhibit no differences as the soaking time increases. This phenomenon indicates that soaking time has no direct influence on the salt mass fraction distribution during the injection stage. The injection stage is dominated by forced convection, and salt ions are carried into the formation along with the advancing injected water. Their distribution is primarily governed by parameters such as the injection pressure differential, injected-water salinity, and reservoir properties. As an operational parameter of the soaking stage, soaking time does not participate in controlling the salt mass fraction distribution during the injection process and thus cannot alter the characteristics of the salt mass fraction field in that stage. Therefore, adjusting the soaking time does not affect the salt mass fraction distribution during the injection stage; differences in the salt mass fraction field only manifest during the subsequent soaking and production stages.

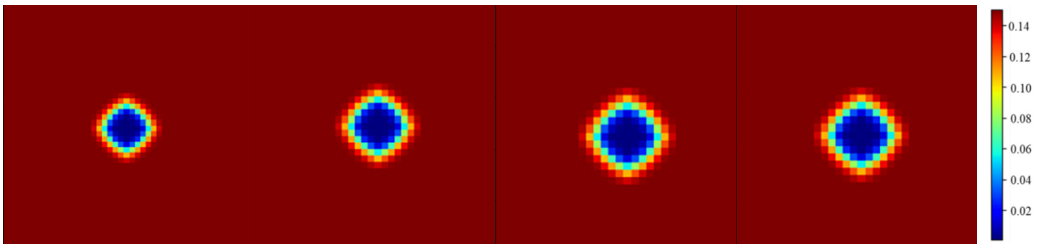


(**a**) 20 d (**b**) 40 d (**c**) 60 d (**d**) 80 d

Figure 29. Salt mass fraction distribution maps during the injection stage under different soaking times.

Figure 30 shows the contour maps of salt mass fraction distribution during the soaking stage under different soaking times. As the soaking time extends from 20 d to 80 d, the central low-salinity zone expands continuously. The salt mass fraction transition zone also gradually widens, and the degree of homogenization of the salt mass fraction field steadily improves. During the soaking stage, injection ceases and salt ion transport is dominated by molecular diffusion, with ions migrating toward the low-salinity region. At 20 d, diffusion has just commenced, and the low-salinity zone is confined to a small area near the wellbore. The period of 40–60 d represents a phase of rapid diffusion development, during which the salt mass fraction field changes noticeably. By 80 d, diffusion has essentially stabilized, and the rate of improvement slows. The longer the soaking time, the more thoroughly the formation water and the injected water mix. Reasonably extending the soaking time can enhance the uniformity of the salt mass fraction field, creating favorable conditions

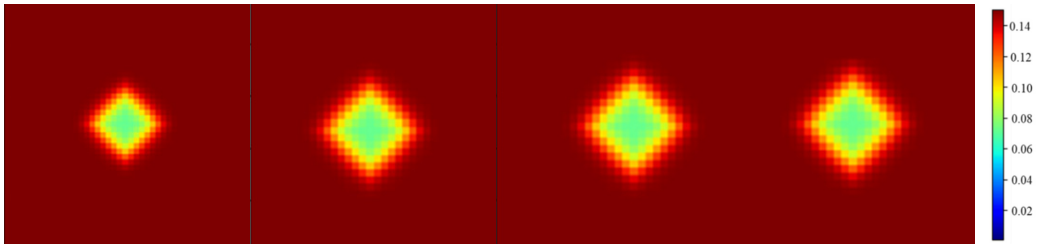
for oil displacement. The improvement in the salt mass fraction field is also conducive to leveraging the oil-displacement advantages of low-salinity water.



(**a**) 20 d (**b**) 40 d (**c**) 60 d (**d**) 80 d

Figure 30. Salt mass fraction distribution maps during the soaking stage under different soaking times.

Figure 31 displays the contour maps of salt mass fraction distribution during the production stage under different soaking times. As the soaking time increases from 20 d to 80 d, the extent of the low salt mass fraction zone during the production stage exhibits a clear expanding trend. When the soaking time is short, salt ion diffusion is insufficient, resulting in a small low salt mass fraction zone and a relatively high near-wellbore salt mass fraction during the production stage. As the soaking time lengthens, the diffusion during the soaking stage becomes more complete, forming a broader mixed low salt mass fraction zone. The salt mass fraction field during the production stage is a direct continuation of the diffusion outcome from the soaking stage. After the well is opened for production, the influence of high-salinity water replenishment from the far field is weakened, allowing the low-salinity zone to be maintained and expanded. Under the 80 d soaking condition, the near-wellbore salt mass fraction during the production stage is the lowest, and the influence range of the low salt mass fraction zone is the widest. The low-salinity baseline established by sufficient soaking is more conducive to leveraging the oil-displacement advantages of low-salinity water. The expansion of the low-salinity zone can promote ion exchange and wettability improvement, enhancing the oil-phase mobilization efficiency. Reasonably extending the soaking time can optimize the salt mass fraction field distribution during the production stage and improve the development performance.



(**a**) 20 d (**b**) 40 d (**c**) 60 d (**d**) 80 d

Figure 31. Salt mass fraction distribution maps during the production stage under different soaking times.

Under the conditions of an injection rate of 80 m^3/d and an injected-water salinity of 1000 mg/L, soaking time has a significant influence on the development performance of low-salinity water huff-and-puff in tight oil reservoirs. As shown in Table 4, with the soaking time extended from 20 d to 80 d, the recovery factor exhibits a continuously increasing trend, but the incremental gain displays a clear pattern of phased attenuation: at a soaking time of 20 d, the recovery factor is 9.32%; extending it to 40 d substantially raises the recovery factor to 10.94%, an increase of 1.62 percentage points. Beyond 40 d, the rate of improvement drops sharply, with the recovery factor reaching only 11.42% at 80 d.

Table 4. Oil recovery under different soaking time conditions.

No.	Huff-and-Puff Cycle	Soaking Time (d)	Cumulative Oil Production (m^3)	Recovery Factor (%)
1	1	20	7411.36	9.32
2	1	40	8699.61	10.94
3	1	60	8922.26	11.22
4	1	80	9081.31	11.42

The soaking stage is the core period for spontaneous imbibition driven by osmotic pressure. When the soaking time is insufficient, the injected water does not fully accomplish matrix imbibition displacement, leaving a substantial amount of mobile oil trapped within the pores. A soaking time of 40 d ensures that the principal imbibition displacement is essentially completed. After 40 d, the crude oil in large pores has been largely produced, and the remaining oil is concentrated in hard-to-mobilize zones such as micropores, where imbibition resistance rises sharply. Further extending the soaking time yields extremely low marginal benefit and may increase the risk of formation damage. Comprehensively considering the oil-enhancement effect and development economics, 40 d is identified as the optimal soaking time for single-cycle low-salinity water huff-and-puff in this tight oil reservoir.

5. Discussion

Based on the parameter sensitivity analysis, the optimal values for the three key parameters are summarized below, independent of the conclusions.

Injected-water salinity. The 1000 mg/L case yields the highest recovery (10.94%) and the largest swept volume. Lower salinity creates a stronger osmotic pressure gradient (approximately 3.9 MPa), which acts synergistically with capillary pressure (2.0–5.0 MPa) to promote spontaneous imbibition during soaking. Thus, 1000 mg/L is the optimal salinity within the tested range.

Injection rate. Recovery decreases with increasing injection rate. The 40 m^3/d case gives the highest recovery (11.13%), but the 80 m^3/d case achieves nearly the same result (10.94%, only 0.19 percentage points lower) while halving the injection time. Considering the balance between recovery and development efficiency, 80 m^3/d is recommended as the preferred rate. Excessively high rates reduce swept volume and recovery; excessively low rates prolong the cycle and reduce economic viability.

Soaking time. Recovery increases from 9.32% at 20 d to 10.94% at 40 d, representing the most efficient imbibition period. Beyond 40 d, incremental gains diminish markedly: only 0.28 percentage points from 40 d to 60 d and 0.20 percentage points from 60 d to 80 d. Therefore, 40 d is identified as the optimal soaking time.

In summary, the recommended parameters are: salinity of 1000 mg/L, injection rate of 80 m^3/d, and soaking time of 40 d, with site-specific adjustments as needed.

6. Conclusions

This paper addresses the commonly overlooked issue of osmotic pressure effects during low-salinity water huff-and-puff in tight oil reservoirs. A mathematical model for water huff-and-puff in tight oil reservoirs considering the effect of low-salinity water was established, and the influences of injected-water salinity, injection rate, and soaking time on the distributions of pore pressure, water saturation, and salt concentration were systematically investigated. The following main conclusions are drawn:

1. Injected-water salinity is the key parameter controlling the osmotic pressure effect during the soaking stage. During the injection stage, convection dominates and the

salinity effect is negligible; capillary pressure acts synergistically with osmotic pressure during the soaking stage, promoting spontaneous imbibition and fluid redistribution. A lower salinity results in a larger concentration difference relative to the formation water, leading to a stronger osmotic driving force and higher oil recovery. In this study, the injected-water salinity of 1000 mg/L yields the highest recovery factor.

2. Both injection rate and soaking time exhibit optimal ranges. An excessively high injection rate tends to reduce the swept volume and cause rapid near-wellbore pressure buildup, whereas a moderately low injection rate (e.g., 40 m^3/d) can enhance matrix imbibition and sweep efficiency, leading to a higher recovery factor; however, an excessively low rate prolongs the injection cycle and may reduce economic viability. Therefore, an optimal injection rate should be determined by balancing development efficiency and economic considerations. The early soaking stage is the efficient period for spontaneous imbibition driven by osmotic pressure; extending the soaking time can effectively enhance oil recovery, but beyond 40 d, further extension yields very limited incremental recovery.
3. The role of osmotic pressure differs significantly across the huff-and-puff stages: it is negligible during the injection stage due to convection dominance, weakens during the production stage as the pressure gradient recovers, and fully exerts its secondary displacement role during the soaking stage, becoming the dominant mechanism governing fluid redistribution and residual oil displacement. The proposed model is capable of characterizing the low-salinity water huff-and-puff behavior under osmotic pressure and can provide theoretical support for the optimization of relevant process parameters in tight oil reservoirs.

Author Contributions: Conceptualization, X.L. and T.Y.; methodology, Z.D.; software, not applicable; validation, X.L.; formal analysis, X.L.; investigation, X.L.; resources, X.L.; data curation, Y.R.; writing—original draft preparation, X.L. and Y.C.; writing—review and editing, X.L.; visualization, not applicable; supervision, X.L. and T.Y.; project administration, X.L.; funding acquisition, X.L. All authors have read and agreed to the published version of the manuscript.

Funding: This work was supported by the National Natural Science Foundation of China (Grant No. 52374038 and U23B2089) and the Innovation Capability Support Program of Shaanxi (Program No. 2024ZC-KJXX-064).

Data Availability Statement: Raw data and derived data supporting the findings of this study are available from the corresponding author, Yu Chen (cyyc2517@163.com), on request.

Conflicts of Interest: The authors declare that they have no known competing financial interests or personal relationships that could have appeared to influence the work reported in this paper.

References

1. Mwakipunda, G.C.; Ngata, M.R.; Yang, Y.; Ma, C. A critical review on low salinity waterflooding for enhanced oil recovery: Experimental studies, simulations, and field applications. *Geoenergy Sci. Eng.* **2023**, *227*, 211936. [CrossRef]
2. Marquez, R.; Ding, H.; Barrios, N.; Liu, Y.; Okuno, R. Recent advances in enhanced oil recovery with low-salinity waterflooding and its hybrid methods in carbonate reservoirs. *Energy Fuels* **2025**, *39*, 8769–8799. [CrossRef]
3. Qu, S.Y.; Jiang, H.Q.; Li, J.J.; Ma, K.J.; Liu, T.Z. Study on influencing factors of enhanced oil recovery by low salinity water flooding. *Appl. Chem. Ind.* **2021**, *50*, 305–310. [CrossRef]
4. Liu, X.; Zhou, D.S.; Shi, Y.H.; Li, M.; Zhang, Z. Mathematical model of imbibition in tight sandstone reservoirs considering osmotic pressure. *Pet. Geol. Recovery Effic.* **2018**, *25*, 93–98. [CrossRef]
5. Morrow, N.R.; Buckley, J.S. Improved oil recovery by low-salinity waterflooding. *J. Pet. Technol.* **2011**, *63*, 106–112. [CrossRef]
6. Lv, X.G.; Li, W. Feasibility study and technical countermeasures for enhanced oil recovery in waterflooding reservoirs at ultra-high water cut stage. *Pet. Geol. Recovery Effic.* **2022**, *29*, 130–137. [CrossRef]
7. Wu, J.; Chang, Y.W.; Li, J.; Wu, Z.H.; Wang, Y.F. Mechanism and applicable conditions of low salinity water flooding technology. *J. Southwest Pet. Univ. (Sci. Technol. Ed.)* **2015**, *37*, 145–151.

8. Morrow, N.R. Wettability and its effect on oil recovery. *J. Pet. Technol.* **1990**, *42*, 1476–1484. [CrossRef]
9. Bigdeli, A.; Thyne, G.; Ulyanov, V. Low salinity water flooding (LSWF), can we move forward? The economic case. *J. Resour. Recovery* **2023**, *1*, e701256. [CrossRef]
10. Liu, X.; Ren, Y.; Wang, N.; Cui, Y.; Du, Z. The influence of pore throat structure on fluid displacement in tight oil reservoir. *Discov. Appl. Sci.* **2026**. [CrossRef]
11. Deng, J.G.; Jiang, Y.; Xu, P.C.; Sun, H.; Li, Y. Enhanced oil recovery by low salinity water flooding based on wettability alteration. *Contemp. Chem. Ind.* **2024**, *53*, 1351–1356. [CrossRef]
12. Liu, X.; Yan, L.; Gao, Q.; Liu, Y.; Huang, H.; Liu, S. Effect of Salinity on the Imbibition Recovery Process of Tight Sandstone Reservoirs. *Processes* **2022**, *10*, 228. [CrossRef]
13. Nyah, F.; Ridzuan, N.; Ikechukwu Nwaichi, P.; Umunnawuike, C.; Agi, A. Comprehensive review on the role of salinity on oil recovery mechanisms during chemical flooding. *J. Mol. Liq.* **2024**, *415*, 126308. [CrossRef]
14. Qian, Z.; Li, H.; Qiao, L.; Shi, L.J.; Chen, X. Experimental study on mechanism of low salinity water flooding in carbonate reservoirs. *Lithol. Reserv.* **2020**, *32*, 159–165.
15. Liu, X.; Cheng, Y.; Peng, L.; Zhang, W.; Li, H. Mechanism of hydrogen bonding at oil–water interfaces on crude oil migration under nanoconfinement. *Processes* **2026**, *14*, 343. [CrossRef]
16. Xie, Q.; Liu, F.H.; Chen, Y.Q.; Liu, B.; Saeedi, A. Effect of electrical double layer and ion exchange on low salinity EOR in a pH controlled system. *J. Pet. Sci. Eng.* **2019**, *174*, 418–424. [CrossRef]
17. Liu, X.; Yao, T.; Cui, Y.; Wang, S.; Li, P. A study on the micro-scale flow patterns and ion regulation mechanisms in low-salinity water flooding. *Energies* **2026**, *19*, 509. [CrossRef]
18. Tang, G.Q.; Morrow, N.R. Influence of brine composition and fines migration on crude oil/brine/rock interactions. *J. Pet. Sci. Eng.* **1999**, *24*, 99–111.
19. Nasralla, R.A.; Nasr-El-Din, H.A. Double-layer expansion: Is it a primary mechanism of improved oil recovery by low-salinity waterflooding? *SPE Reserv. Eval. Eng.* **2014**, *17*, 49–59.
20. Arain, A.H.; Negash, B.M.; Yekeen, N.; Farooqi, A.S.; Alshareef, R.S. Synergising nanoparticles and low salinity waterflooding for enhanced oil recovery: A state-of-the-art review. *J. Mol. Liq.* **2024**, *400*, 124495. [CrossRef]
21. RezaeiDoust, A.; Puntervold, T.; Strand, S.; Austad, T. Smart water as wettability modifier in carbonate and sandstone: A discussion of similarities/differences in the chemical mechanisms. *Energy Fuels* **2009**, *23*, 4479–4485. [CrossRef]
22. Sandengen, K.; Arntzen, O.J. Osmosis during low salinity water flooding. In *EAGE 17th European Symposium on Improved Oil Recovery, St. Petersburg, Russia, 2013*; European Association of Geoscientists & Engineer: Bunnik, The Netherlands, 2013.
23. Wei, X.M.; Zhang, Y.Y.; Jiang, W.C.; Hou, J.; Chen, Z. Experiment on effect of clay mineral type on recovery factor of low salinity water flooding. *Pet. Geol. Oilfield Dev. Daqing* **2022**, *41*, 120–129. [CrossRef]
24. Bernard, G.G. Effect of floodwater salinity on recovery of oil from cores containing clays. In Proceedings of the Presented at the SPE California Regional Meeting, Los Angeles, CA, USA, 26–27 October 1967. SPE 1725.
25. Li, X.J.; Fu, M.L.; Chen, H.; Yang, S.; Zhao, L. Experimental study on mechanism of smart water flooding for enhanced oil recovery in sandstone reservoirs. *Pet. Geol. Recovery Effic.* **2018**, *25*, 101–106. [CrossRef]
26. Sandengen, K.; Kristoffersen, A.; Melhuus, K.; Jøsang, L.O. Osmosis as mechanism for low-salinity enhanced oil recovery. *SPE J.* **2016**, *21*, 1227–1235. [CrossRef]
27. Fredriksen, S.B.; Rognmo, A.U.; Fernø, M.A. Pore-scale mechanisms during low salinity waterflooding: Oil mobilization by diffusion and osmosis. *J. Pet. Sci. Eng.* **2018**, *163*, 650–660. [CrossRef]
28. Fakcharoenphol, P.; Kurtoglu, B.; Kazemi, H.; Charoenwongsa, S. The effect of osmotic pressure on improve oil recovery from fractured shale formations. In Proceedings of the SPE Unconventional Resources Conference, The Woodlands, TX, USA, 1–3 April 2014.
29. Huang, Y.; Dai, C.; Chen, Z.; Sun, Y.; Zhao, M.; You, Q. Probing the mechanism of in situ oil droplet swelling during low salinity water flooding. *Colloids Surf. A* **2022**, *636*, 128133. [CrossRef]
30. Zhao, C.; Wang, Q.; Zhao, J.; Zhang, Y.; Li, H. An understanding of oil–water replacement mechanism based on interfacial tension gradient during the well shut-in. *Energy Rep.* **2022**, *8*, 4006–4021. [CrossRef]
31. Takeda, M.; Manaka, M.; Ito, D. Experimental evidence of chemical osmosis-driven improved oil recovery in low-salinity water flooding: Generation of osmotic pressure via oil-saturated sandstone. *J. Pet. Sci. Eng.* **2022**, *215*, 110731. [CrossRef]
32. Bui, B.T.; Tutuncu, A.N. Contribution of osmotic transport on oil recovery from rock matrix in unconventional reservoirs. *J. Pet. Sci. Eng.* **2017**, *157*, 392–408. [CrossRef]
33. Liu, X.; Yao, T.; Gong, Y.; Liu, S.; Li, H. Microscopic mechanisms and dominant productivity controls of frac-driven oil recovery in tight reservoirs. *Pet. Sci. Technol.* **2026**, 1–19. [CrossRef]
34. Wang, X.; Wu, X.; Shi, L.; Ogaidi, A.R.S.; Shan, X.; Ye, Z.; Qin, G.; Liu, J.; Wu, B. Application of low-salinity waterflooding in heavy oil sandstone reservoir: Oil recovery efficiency and mechanistic study. *ACS Omega* **2024**, *9*, 30782–30793. [CrossRef] [PubMed]

35. Fan, P.; Liu, Y.; He, Y.; Hu, Y.; Chao, L.; Wang, Y.; Liu, L.; Li, J. Experimental study on the mechanism and law of low-salinity water flooding for enhanced oil recovery in tight sandstone reservoirs. *ACS Omega* **2024**, *9*, 12665–12675. [CrossRef] [PubMed]
36. Jerauld, G.R.; Webb, K.J.; Lin, C.Y.; Seccombe, J.C. Modeling low-salinity waterflooding. *SPE Res. Eval. Eng.* **2006**, *11*, 1000–1012. [CrossRef]
37. Omekeh, A.; Friis, H.A.; Fjelde, I.; Evje, S. Modeling of ion-exchange and solubility in low salinity water flooding. In *SPE Improved Oil Recovery Symposium*; SPE: Richardson, TX, USA, 2012.
38. Apolinário, F.O.; Pires, A.P. Mathematical modeling of low salinity waterflooding in sandstone reservoirs: Enhanced oil recovery by multicomponent cation exchange. *Chem. Eng. Res. Des.* **2023**, *193*, 725–737. [CrossRef]
39. Jalilian, M.; Mahdavi, S.; Pourafshary, P.; You, Z.; Mohammadi, A.H. Assessing the impact of geochemical mechanism and interpolation factor selection on the precision of low-salinity waterflooding modelling: A comparative study. *Geosystem Eng.* **2024**, *27*, 304–318. [CrossRef]
40. Liu, F.; Wang, D.; Hu, Z.; Song, K.; Chen, J.; Zhou, Y.; Niu, W. Pore-scale modeling of low salinity water flooding in porous media using the lattice Boltzmann method. In Proceedings of the SPE Symposium and Exhibition-Production Enhancement and Cost Optimisation, Kuala Lumpur, Malaysia, 3–4 September 2024; Volume 12.
41. Alvarez, A.C.; Bruining, J.; Marchesin, D. Modeling low saline carbonated water flooding including surface complexes. *Comput. Geosci.* **2024**, *28*, 373–393. [CrossRef]
42. He, Y.; Liu, Y.; Zhang, B.; Zhou, L.; Wang, C. Low-salinity water flooding in Middle East offshore carbonate reservoirs: Adaptation to reservoir characteristics and dynamic recovery mechanisms. *Phys. Fluids* **2025**, *37*, 076605. [CrossRef]
43. Gbadamosi, A.; Patil, S.; Al Shehri, D.; Kamal, M.S.; Hussain, S.M.S.; Al-Shalabi, E.W.; Hassan, A.M. Recent advances on the application of low salinity waterflooding and chemical enhanced oil recovery. *Energy Rep.* **2022**, *8*, 9969–9996. [CrossRef]
44. Marine, I.W.; Fritz, S.J. Osmotic model to explain anomalous hydraulic heads. *Water Resour. Res.* **1981**, *17*, 73–82. [CrossRef]
45. Brooks, R.H.; Corey, A.T. *Hydraulic Properties of Porous Media*; Hydrology Papers; No. 3; Colorado State University: Fort Collins, CO, USA, 1964.

Disclaimer/Publisher's Note: The statements, opinions and data contained in all publications are solely those of the individual author(s) and contributor(s) and not of MDPI and/or the editor(s). MDPI and/or the editor(s) disclaim responsibility for any injury to people or property resulting from any ideas, methods, instructions or products referred to in the content.